

V. Theory of Measurement Feedback Based Quantum Neural Networks

In this Chapter, we present the theory of quantum neural networks connected by a measurement feedback circuit, which have been recently demonstrated independently at NTT [1] and Stanford University [2]. As an earlier study, the non-degenerate optical parametric oscillators with idler-measurement and signal-feedback control was theoretically studied in the context of generating various quantum states of light, such as coherent states, squeezed states and photon number states [3]. Those three specific states are generated by optical heterodyne detection, homodyne detection and photon number detection, respectively. The semiconductor lasers with junction voltage-measurement and injection current-feedback control was experimentally studied in the context of generating number-phase squeezed states of light [4]. An indirect quantum measurement using a probe, treated in the previous Chapter IV, plays a central role in such measurement-feedback oscillator systems. The concept can be extended here to implement the NP-hard Ising problems and NP-complete k -SAT problems in quantum neural networks [1, 2]. Two complementary theories will be presented: one is directly based on the density operator master equation in in-phase amplitude eigenstate $|x\rangle$ representation and the homodyne measurement projectors [5], while the other utilizes the c -number stochastic differential equations (CSDE) derived by the positive $P(\alpha, \beta)$ representation of the density operator and the replicator dynamics [6].

5.1 A quantum model based on density operator master equations and homodyne measurement projectors

5.1.1 Theoretical formulation

Our theoretical model consists of four optical components; a PPLN waveguide as a phase sensitive amplifier, two output couplers for stimulating a measurement loss and background loss, and a feedback circuit consisting of optical homodyne detectors, analog-to-digital converter (ADC), field programmable gate array (FPGA), digital-to-analog converter (DAC) and optical amplitude/phase modulator (Fig. 1). The first output coupler represents the background loss in the QNN ring cavity. A part of the signal pulse is extracted with the second output coupler and used to measure the in-phase amplitude of the intra-cavity signal pulse by homodyne detectors. In the feedback circuit, the feedback pulses are generated as

coherent states with an average excitation amplitude proportional to $x_i = \sum_j J_{ij} \tilde{x}_j$, where \tilde{x}_j is the measurement result (inferred value for \hat{x}_j) for the j -th pulse and J_{ij} is the Ising coupling constant determined by a given problem instance. Each signal pulse experiences these four processes every time it goes one round trip along the ring cavity. To simulate how the quantum states of signal pulses evolve, we calculated the completely positive trace preserving (CPTP) maps. Then, we numerically simulate the system by expanding the field density operators with the eigen-vectors of the in-phase amplitude operator $\hat{x} = (a + a^\dagger) / \sqrt{2}$ [7], where a, a^\dagger is the annihilation/creation operator of the signal pulse. Because these four processes along the ring cavity are local operations and classical communications (LOCC), the states of the signal pulses are separable and not entangled. This is in sharp contrast to the optical delay line coupling DOPO network [8, 9]. We calculated the conditional density matrices governed by the randomly determined but specific measurement results x_m of the in-phase amplitudes of the signal pulses extracted by the second output coupler.

In the following subsections, we derive the time evolution equation for the density operator and CPTP maps for those four processes in the ring cavity. For simplicity, we take the rotating coordinate and ignore the free field Hamiltonian.

A. Phase sensitive amplifier (PSA)

In the PSA, the signal pulse in an initial state $\hat{\rho}$ and with a frequency ω and annihilation operator \hat{a} interacts with the pump pulse in an initial coherent state $|\beta\rangle$ and with a frequency 2ω and annihilation operator \hat{b} . We properly choose the coordinate of the phase space in order that β is real.

The Hamiltonian for the parametric interaction in the PSA is written as

$$\hat{\mathcal{H}} = \frac{1}{2} \left(e^{2i\omega t} a^{\dagger 2} \hat{B} + e^{-2i\omega t} a^2 \hat{B}^\dagger \right). \quad (1)$$

Here, \hat{B} is defined as

$$\hat{B} = i \sum_{\omega_k} g(\omega_k) e^{-i\omega_k t} \hat{b}(\omega_k), \quad (2)$$

where $\hat{b}(\omega_k)$ is the annihilation operator of the pump field of frequency ω_k , and $g(\omega_k)$ is a parametric coupling constant. Initially, the pump field at 2ω is in a coherent state $|\beta\rangle$ and

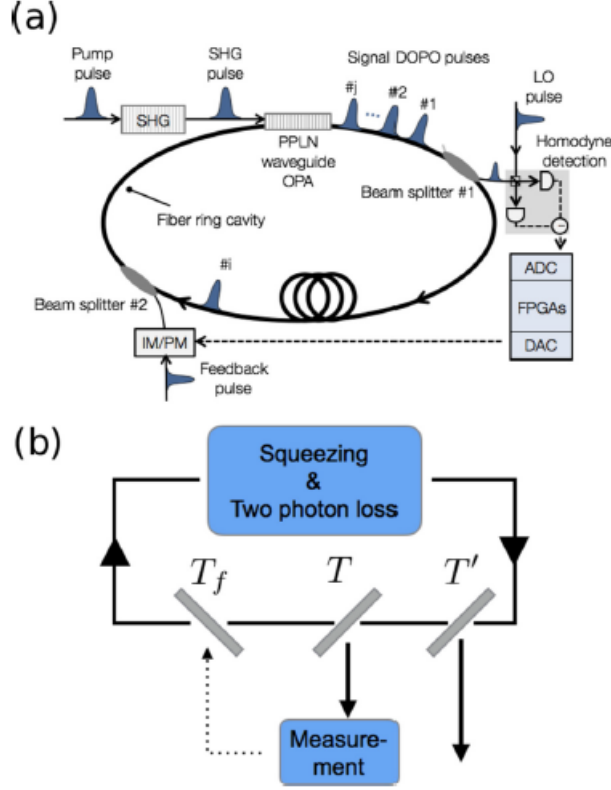


FIG. 1: (a) The experimental set up of the quantum neural network (QNN) using the degenerate optical parametric oscillators and the discrete-time measurement feedback circuit. (b) The corresponding theoretical model [5].

all the other frequency modes at $\omega_k \neq 2\omega$ are assumed to be vacuum states $|0\rangle$. When we translate the coordinate of the phase space of the pump field as,

$$\hat{b} \rightarrow \hat{b} + \beta,$$

we can interpret that the initial state of the pump field is also a vacuum state in the new coordinate. In this case, the Hamiltonian (Eq.(1)) is rewritten as

$$\begin{aligned} \hat{\mathcal{H}} &= g(2\omega) \frac{i}{2} (\hat{a}^{\dagger 2} \beta - \hat{a}^2 \beta^*) + \frac{1}{2} \left(e^{2i\omega t} \hat{a}^{\dagger 2} \hat{B} + e^{-2i\omega t} \hat{a}^2 \hat{B}^\dagger \right) \\ &=: \hat{\mathcal{H}}_s + \hat{\mathcal{H}}_{\text{int}}. \end{aligned} \quad (3)$$

We shall think that the first term $\hat{\mathcal{H}}_s$ represents the linear phase sensitive amplification/deamplification (squeezing effect) by the coherent pump field. This part of the Hamiltonian can be absorbed as a Hamiltonian of the signal. The second part is expressed as

$$\hat{\mathcal{H}}_{\text{int}}^I = \frac{1}{2} \left(e^{2i\omega t} \hat{a}^{I\dagger 2} (t) \hat{B} + e^{-2i\omega t} \hat{a}^{I2} (t) \hat{B}^\dagger \right), \quad (4)$$

in the interaction picture. Taking the Born-Markov approximation and the rotating wave approximation, we can find the master equation corresponding to the interaction Hamiltonian as [10],

$$\begin{aligned} \frac{d\hat{\rho}^I}{dt} = & \sum_k [(\Gamma_k + \Gamma_k^*) \hat{a}^{I2} \hat{\rho}^I \hat{a}^{I\dagger 2} (t) \\ & - \Gamma_k \hat{a}^{I2} (t) \hat{a}^{I\dagger 2} (t) \hat{\rho}^I - \Gamma_k^* \hat{\rho}^I \hat{a}^{I\dagger 2} (t) \hat{a}^{I2} (t)], \end{aligned} \quad (5)$$

where $\int dt \int ds e^{-(t+s)} t^{(n-1)} s^{(m-1)} < DT >$

$$\begin{aligned} \Gamma_k &= \int_0^\infty ds e^{i(2\omega - \omega_k)s} g(\omega_k)^2 \langle \hat{b}(\omega_k) \hat{b}^\dagger(\omega_k) \rangle \\ &= \frac{g^2}{2} \delta(2\omega - \omega_k) \langle \hat{b} \hat{b}^\dagger \rangle \\ &= \frac{g^2}{2} \delta(2\omega - \omega_k). \end{aligned} \quad (6)$$

When we go back to the Schrödinger picture, the master equation for the PSA is finally given by

$$\begin{aligned} \frac{d\hat{\rho}}{dt} = & \frac{g\beta}{2} [(\hat{a}^{\dagger 2} - \hat{a}^2), \hat{\rho}] \\ & + \frac{g^2}{2} [2\hat{a}^2 \hat{\rho} \hat{a}^{\dagger 2} - \hat{a}^{\dagger 2} \hat{a}^2 \hat{\rho} - \hat{\rho} \hat{a}^{\dagger 2} \hat{a}^2]. \end{aligned} \quad (7)$$

The first term of Eq.(7) represents a standard unitary (squeezing/anti-squeezing) process, while the second term is a Lindblad form representing the two photon loss process associated with the parametric pump photon generation. We defined the squeezing rate $S = g\beta t$ and two photon loss rate $L = g^2 t$, where t is the time duration of this interaction in the PSA. The linear gain G in terms of the energy of the signal pulse can be represented as $G = \exp(2S)$. One of the important assumption leading to Eq.(7) is that the gain saturation (or pump depletion) is relatively weak, i.e. the signal pulse grows its power and depletes the pump power only slightly, instead of depleting the pump power completely as is the case for a strong signal-pump interaction [11]. The other important assumption is that the pump field is dissipated into external reservoirs each time of PSA and a fresh coherent state pump field $|\beta\rangle$ is prepared for the next round of PSA.

The working equation for our numerical simulation is obtained by expanding the density operator $\hat{\rho}$ in terms of the in-phase amplitude eigenstates $|x\rangle$:

$$\begin{aligned}
\frac{d}{dt} \langle x | \hat{\rho} | x' \rangle = & g\beta (-z\partial_z - w\partial_w - 1) \langle x | \hat{\rho} | x' \rangle \\
& + \frac{g^2}{8} (-z^2w^2 + 3(z^2 + w^2)) \\
& + (z^2 - w^2 + 8) (z\partial_z + w\partial_w) + 4(z^2 - 1) \partial_z^2 \\
& + 4(w^2 - 1) \partial_w^2 + 4(z\partial_z - w\partial_w) (\partial_z^2 - \partial_w^2) \\
& - 4\partial_z^2\partial_w^2 \langle x | \hat{\rho} | x' \rangle,
\end{aligned} \tag{8}$$

where $z = x + x'$ and $w = x - x'$.

B. Output couplers and homodyne detectors

A part of the signal pulse energy is extracted from the ring cavity with two beam splitters. At the first output coupler, the extracted signal-field is simply dissipated in external reservoirs, which represents the background linear loss of the ring cavity. At the second output coupler, the in-phase amplitude $\hat{x} = (\hat{a} + \hat{a}^\dagger) / \sqrt{2}$ of the extracted field is projectively measured by homodyne detectors. We define the transmittance of the second and first beam splitters as $T = \sin^2 \theta$ and $T' = \sin^2 \theta'$. When the signal pulse goes into the beam splitter, it is combined with the incident vacuum state from external environments. Thus, the measurement by the homodyne detectors has a finite measurement error, which comes from the vacuum fluctuation. We define the annihilation operators of the signal and the vacuum field as \hat{a} and \hat{a}_{vac} . Then, the output field annihilation operators can be written by the unitary operator \hat{U} of the beam splitter with a parameter θ :

$$\hat{U}^\dagger \hat{a} \hat{U} = \sin \theta \hat{a}_{\text{vac}} + \cos \theta \hat{a} \tag{9}$$

$$\hat{U}^\dagger \hat{a}_{\text{vac}} \hat{U} = \sin \theta \hat{a} + \cos \theta \hat{a}_{\text{vac}} \tag{10}$$

From these equations, the projection operator for the intra-cavity signal field, corresponding to the measured value of x_m , can be expressed as below:

$$\begin{aligned}
\hat{M}_{x_m} &= \langle x_m | \hat{U} | 0 \rangle \\
&= \int dx_i dx_f \pi^{-1/4} \delta(x_i - (\cos \theta x_f + \sin \theta x_m)) \\
&\quad \times \exp\left(-\frac{1}{2}(-\sin \theta x_f + \cos \theta x_m)^2\right) |x_f\rangle \langle x_i|
\end{aligned} \tag{11}$$

To calculate the conditional density matrix for the post-measurement state, we generate a random number and determine a measured value x_m according to the probability of $P(x_m) = \text{Tr}(\hat{M}_{x_m} \hat{\rho} \hat{M}_{x_m}^\dagger)$. When we do not measure the extracted fields, which is the case for the first output coupler, the relevant operator is,

$$\int_x \mathcal{L}(\hat{M}_x) \mathcal{R}(\hat{M}_x^\dagger) dx, \tag{12}$$

where \mathcal{L} and \mathcal{R} mean the left and right action as a super operator.

C. Feedback process

In the injection feedback process, the signal pulse and the feedback pulse, which is prepared in a coherent state $|\alpha\rangle$, are combined with a third beam splitter. The transmittance of the third beam splitter, defined as $T_f = \sin^2 \theta_f$, is very low and the change of the density matrix of the intra-cavity signal pulse is described by a simple displacement operator, $\hat{D}(\alpha\theta_f) = \exp(\alpha\theta_f \hat{a}^\dagger - \alpha^* \theta_f \hat{a})$. In the Heisenberg picture, the in-phase amplitude operator \hat{x} will be translated as $\hat{D}(\alpha\theta_f) \hat{x} \hat{D}^\dagger(\alpha\theta_f) = x + \alpha\theta_f/\sqrt{2}$.

The amplitude of the feedback pulse α is determined with the measured values of the homodyne detectors. We define the feedback rate R as a ratio of $\alpha\theta_f/\sqrt{2}$ to the in-phase amplitude \hat{x} of the intra-cavity signal pulse estimated with the measured value x_m by the homodyne detectors.

D. Summary of the model

In summary, the signal pulses experience these four non-unitary processes during one loop along the ring cavity. This system is described by five physical parameters; linear gain G (or squeezing rate S), two photon loss rate L , the background linear loss rate $1 - T'$, the measurement linear loss rate $1 - T$, and the feedback rate R . The total net gain during

the one round trip along the cavity is $G_{tot} = G \times T \times T'$, where we assume $T_f \simeq 0$. For the following numerical simulations, we expand conditional density matrices of pulses with x -eigenvectors. Note that the elements of density matrices $\langle x | \hat{\rho} | x' \rangle$ are real numbers in this system.

In the following section, we will plot density matrices as functions of $x + x'$ and $x - x'$. Figure 2 shows the contour maps of the density matrices corresponding to four typical quantum states. The line of $x - x' = 0$ (horizontal cut) is the diagonal elements of a density matrix and represents the probability distribution on x . The vacuum state can be represented with a gaussian function whose variance is $\langle \Delta \hat{x}^2 \rangle = 0.5$ (Fig. 2(a)) and when a vacuum state is anti-squeezed along the x -axis, it becomes broader gaussian distribution (Fig. 2(b)). While non-zero values appear along the vertical cut of $x + x' = 0$ when two coherent states $|\alpha\rangle$ and $|-\alpha\rangle$ have a quantum coherence as a Schrödinger's cat state $\frac{1}{\sqrt{2}}(|\alpha\rangle + |-\alpha\rangle)$ (Fig. 2(c)), they do not appear when the two coherent states are classically mixed (Fig. 2(d)).

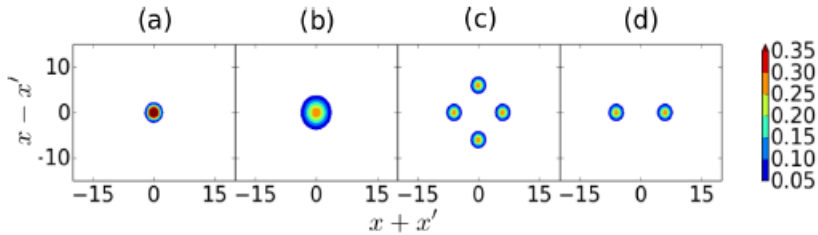


FIG. 2: Contour maps of the density matrices $\langle x | \rho | x' \rangle$ of typical quantum states as functions of $x + x'$ and $x - x'$. (a) a vacuum state (b) a squeezed vacuum state (c) a Schrödinger's cat state of coherent states $\frac{1}{\sqrt{2}}(|\alpha\rangle + |-\alpha\rangle)$ (d) a classical mixture of coherent states $\frac{1}{2}(|\alpha\rangle\langle\alpha| + |-\alpha\rangle\langle-\alpha|)$ [5].

5.1.2 Numerical Simulation Results

We studied the time evolution of the simplest DOPO network consisting of two signal pulses interacting with an anti-ferromagnetic coupling. In this case, the two degenerate ground states are up-down ($|\uparrow\downarrow\rangle$) state and down-up ($|\downarrow\uparrow\rangle$) state.

A. Three steps in optimization process

In this subsection, we assume that the background linear loss in the ring cavity is zero ($T' = 0$) and the transmittance of the output coupler to the homodyne detectors is $T = 0.01$.

Other numerical parameters are given in Table I. Figure 3 shows the time-development of the conditional density matrices of the two signal pulses governed by the sequence of measured values x_m . The initial states of the two pulses are vacuum states (the number of round trips $N = 0$ in Fig. 3(b)). At that time, $\langle \hat{x} \rangle = 0$ and $\langle \Delta \hat{x}^2 \rangle = 0.5$ as shown in Fig. 3(a). There are three stages in the optimization process. In the first stage, the two pulses are anti-squeezed along x -axis by the phase sensitive amplifier and $\langle \Delta \hat{x}^2 \rangle$ are getting broader ($N = 30$ in Fig. 3(b)). Note that not only diagonal x -distribution along x -axis is broadened but also off-diagonal quantum coherence along y -axis is also broadened. In the second stage, because of the gain saturation and the feedback, the expectation values $\langle \hat{x} \rangle$ move to opposite directions, either negative or positive value, ($N = 60$ in Fig. 3(b)). The gain saturation is responsible for spontaneous symmetry breaking at DOPO threshold, while the feedback makes the system to select an anti-ferromagnetic order instead of a ferromagnetic order. Finally, in the third stage, the state is getting close to the highly excited coherent state and $\langle \Delta \hat{x}^2 \rangle$ is reduced to 0.5 (Fig. 3(a) and $N = 150$ in Fig. 3(b)). At this stage, the optimization process of the QNN is completed.

TABLE I: The numerical parameters for simulating the QNN consisting of two DOPO pulses [5].

physical meaning	name	value
Net Gain in One Loop	G_{tot}	1.05
Background Loss Rate	T'	0
Feedback Rate	R	0.005
Two Photon Loss Rate	L	0.002

B. Correlated Schrödinger's cat states and non-Gaussian states

Next, we show the simulation results with various measurement strength $1 - T$ under no background loss $T' = 0$. Parameters for numerical simulations are shown in Table I. Figure 4 shows the conditional density matrices $\langle x | \hat{\rho} | x' \rangle$ governed by the sequence of measurement results x_m . As we can see, the anti-squeezing effect at the early period of the optimization process is bigger when the transmittance of the output coupler is bigger or the measurement strength is weaker. When $T = 0.1$ or $T = 0.5$, the states are slightly anti-squeezed and

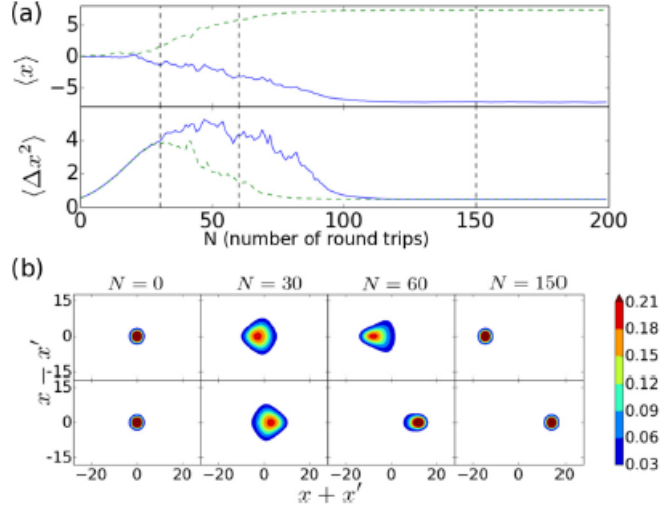


FIG. 3: Time evolution of the conditional density matrices of the two signal pulses governed by the measurement results x_m with $T = 0.01$ and $T' = 0$. Other parameters are shown in Table I. (a) The evolution of $\langle \hat{x} \rangle$ and $\langle \Delta \hat{x}^2 \rangle$. (b) The contour maps of the conditional density matrices $\langle x | \hat{\rho} | x' \rangle$ of the two DOPOs behind the PSA plotted on the coordinate $x - x'$ and $x + x'$. In this system, all elements of the density matrices are real numbers [5].

they are quickly displaced. The DOPO network under such a strong measurement seems to be the closest analog to a classical system, because the time-development of displaced anti-squeezed states could be well approximated with the time evolution of Gaussian states, which are described by the rate of displacement and the rate of anti-squeezing. In the next section, we will show this is not necessarily the case. The states are highly non-Gaussian even if the measurement is strong. When $T = 0.001$, the states maintain the quantum coherence between macroscopically separated "up state" and "down state" (for instance, $N = 60$ in Fig. 4(a)). Those states are actually very close to the Schrödinger's cat state shown in Fig. 2(c). As shown in Fig. 4(e), the Wigner function features the oscillatory behaviors and negative values which manifest the quantum interference between the macroscopically separated "up state" and "down-state". The two cat states possess the opposite centers of gravity, i.e. one is biased toward a positive x value and the other is biased toward a negative x value. They are distinct from an entangled state, $\frac{1}{\sqrt{2}} (|\alpha\rangle |-\alpha\rangle + |-\alpha\rangle |\alpha\rangle)$. The two DOPO fields are separable but yet they are classically correlated Schrödinger's cat state.

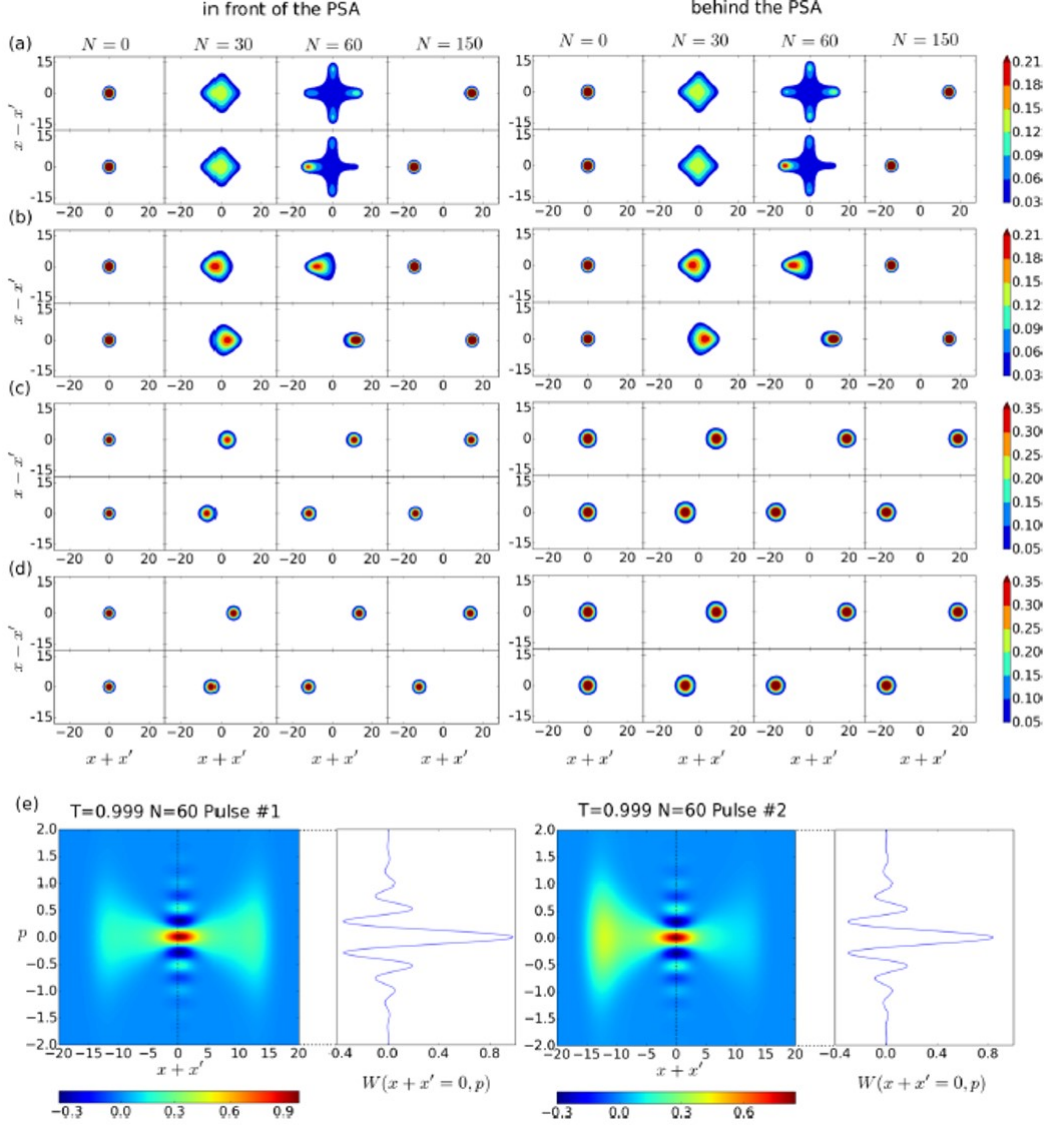


FIG. 4: The contour maps of the conditional density matrices $\langle x | \hat{\rho} | x' \rangle$ of two signal pulses governed by the measurement results x_m with (a) $T = 0.001$, (b) $T = 0.01$, (c) $T = 0.1$, (d) $T = 0.5$ at round trips of $N = 0, 30, 60, 150$ in front of and behind the PSA. Other parameters are shown in Table I. In this system, all elements of the density matrices are real numbers. (e) The Wigner function $P(x + x', p) = \frac{1}{\pi} \int_{-\infty}^{\infty} \langle x | \hat{\rho} | x' \rangle e^{2ip(x-x')} d(x-x')$ of the density matrices at $N = 60$ in Fig. 4(a) [5].

C. Heisenberg limit

Figure 5 shows the uncertainty relationship between $\langle \Delta \hat{x}^2 \rangle$ and $\langle \Delta \hat{p}^2 \rangle$ of a typical conditional density matrix of one signal pulse for various transmittance T . Here, x and p are the in-phase and quadrature-phase amplitudes defined by $\hat{x} = (\hat{a} + \hat{a}^\dagger) / \sqrt{2}$, $\hat{p} = (\hat{a} - \hat{a}^\dagger) / \sqrt{2}i$. The initial vacuum state at $N = 0$ has $\langle \Delta \hat{x}^2 \rangle = \langle \Delta \hat{p}^2 \rangle = 0.5$. As the signal pulses go along the ring cavity for many round trips, $\langle \Delta \hat{x}^2 \rangle$ of a conditional density matrix gets bigger and

then gets smaller to return to $\langle \Delta \hat{x}^2 \rangle = 0.5$. Those lines form loops. The dashed curve represents the minimum uncertainty product, i.e. Heisenberg uncertainty principle dictates $\langle \Delta \hat{x}^2 \rangle \langle \Delta \hat{p}^2 \rangle \geq 1/4$. Because the states are squeezed vacuum states at the early stage of the optimization process, the lines of DOPO pulses in the figure are on this dashed line when $\langle \Delta \hat{x}^2 \rangle$ is relatively small. The numerical results in Fig. 5 clearly show the two facts. The first fact is that when the measurement strength is weaker, the state are more anti-squeezed but the quantum coherence between the "up state" (the region $x > 0$) and the "down state" (the region $x < 0$) is degraded by the cavity loss so that the squeezed noise $\langle \Delta \hat{p}^2 \rangle$ is much larger than the Heisenberg limit. The correlated Schrödinger's cat states shown in Fig. 4(e) belong to this case. The second fact is that as T is getting smaller or the measurement strength becomes stronger, the conditional density matrix is close to the Heisenberg limit. The DOPO state is only slightly non-Gaussian due to the repeated projection induced by the measurements.

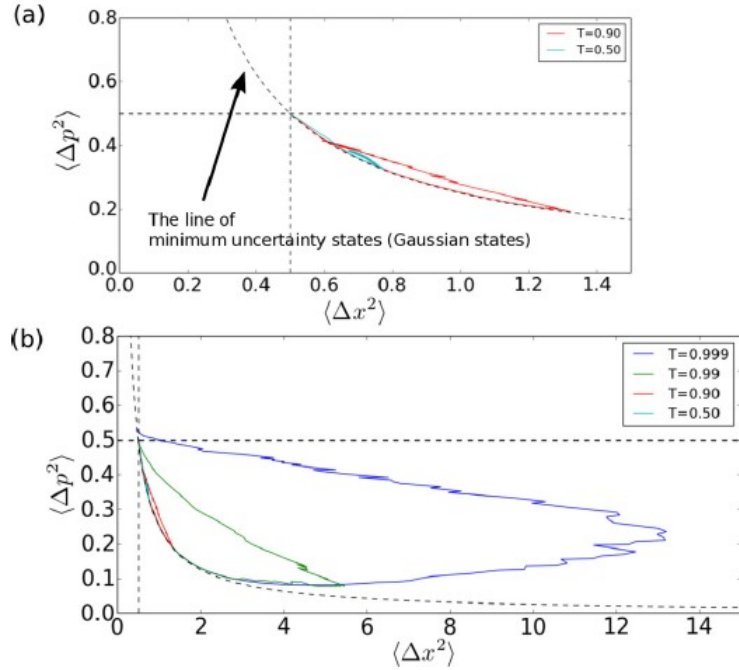


FIG. 5: $\langle \Delta \hat{x}^2 \rangle$ and $\langle \Delta \hat{p}^2 \rangle$ of a typical conditional density matrix of a signal pulse governed by the sequence of randomly determined measurement results x_m , with various strengths of the measurement. The dashed curves are the line of the minimum uncertainty product $\langle \Delta \hat{x}^2 \rangle \langle \Delta \hat{p}^2 \rangle = 0.25$. The horizontal and vertical dashed lines in (a) and (b) represent the standard quantum limit (SQL) which separates non-classical states and classical states, i.e. statistical mixture of coherent states. The initial state of the signal pulse is a vacuum state ($\langle \Delta \hat{x}^2 \rangle = \langle \Delta \hat{p}^2 \rangle = 0.5$)[5].

D. Success rate vs. background loss

We produced many traces of conditional density matrices, in order to calculate how the probability of success P_s of finding a ground state depends on the background loss rate $1 - T'$, with the numerical parameters presented in Table II. Three different time schedules of net gain G_{tot} are assumed. The results are shown in Fig. 6. The success rate is given by $\int_{x_1 x_2 < 0} \langle x_1 | \langle x_2 | \hat{\rho} | x_1 \rangle | x_2 \rangle dx_1 dx_2$, where x_1, x_2 denote the in-phase amplitudes of the two signal pulses and ρ is the full density matrix for the two signal DOPO pulses. The initial success rate for the two vacuum states is 0.5 and as N increases the success rate becomes higher. To see the dependence of the probability of success on the background loss rate and the time schedule of the net gain, we set the feedback rate R not to be sufficiently strong. That is, the feedback pulse power is comparable to competing noise power.

TABLE II: Parameters for the numerically simulation in Fig. 6 [5].

physical meaning	name	value
Measurement Strength	T	0.01
Feedback Rate	R	0.005
Two Photon Loss Rate	L	0.002

In the case of a zero or low background loss ($T' = 0, 0.1$), the initial increasing rate of P_s is smaller than the case of a larger background loss. When the loss rate is low, the fluctuation arising from the anti-squeezed quantum noise is large, which makes the absolute average amplitude $|\langle x \rangle|$ being small compared to the anti-squeezed quantum noise at the early stage. Thus, the in-phase amplitudes of the feedback pulses are also small compared to the anti-squeezed noise, and this leads to a lower increase rate for the probability of success at the early stage.

However, once P_s starts to increase, it suddenly goes up and reaches to the final constant value. The final value greatly depends on the time schedule of the net gain G_{tot} . When G_{tot} increases rapidly, the final success probability P_s becomes lower in the case of low background loss. This is because the small vacuum fluctuation due to small loss leads to the states of the DOPO pulses being easily trapped into the wrong potential wells. On the other hand, when the background loss is large or T' is small ($T' = 0.5, 0.3$), the states are

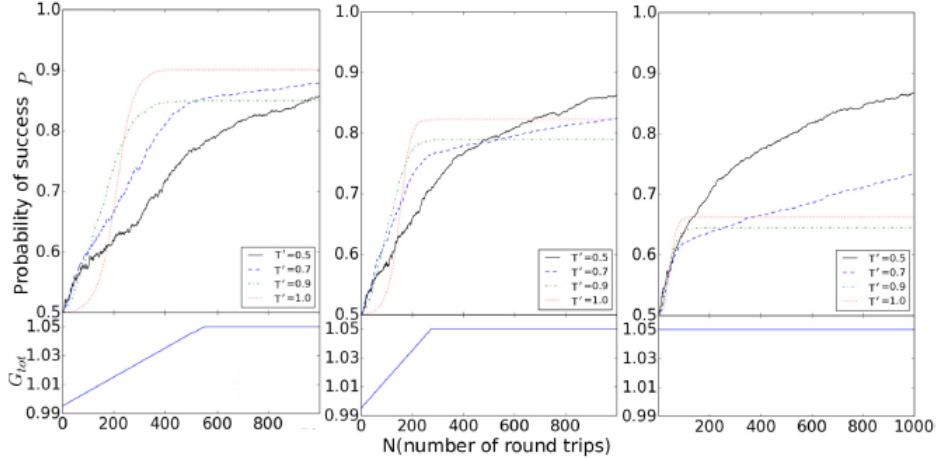


FIG. 6: The probability of success P_s for various background loss rate $1 - T'$ with three net gain schedules. The definition of the success rate is $\int_{x_1 x_2 < 0} \langle x_1 | \langle x_2 | \hat{\rho} | x_1 \rangle | x_2 \rangle dx_1 dx_2$, where x_1, x_2 are the in-phase amplitudes for the two signal pulses. These values are calculated from the averages of the probabilities of 4500 conditional density matrices for $T' = 0.5, 0.3, 0.1, 0$. Other parameters for the numerical simulation are shown in Table II. At around $N = 1000$, because almost all of the probabilities of success of the quantum trajectories are zero or unity, the standard deviation s_P of P_s can be calculated from the random partition distribution $s_P = \sqrt{P(1 - P)/4500} < 0.007$ [5].

fluctuated strongly by vacuum fluctuations and can tunnel from the up (down) state to the down (up) state even after G_{tot} becomes larger than one (above the threshold). Thus, the success rates P_s continue to increase at above the threshold.

If the DOPO network has a high-Q cavity, it is better to increase the pump rate slowly to ensure the system has an enough time for quantum parallel search at below threshold. On the other hand, if the DOPO network has a low-Q cavity, it is better to increase the pump rate rapidly to ensure the system has an enough time for quantum tunneling at above threshold.

5.2 A quantum model based on c -number stochastic differential equations and replicator dynamics

In this section, we will derive the master equation of the continuous wave (CW) measurement-feedback QNN. For the sake of simplicity, we describe the derivation of the master equations for only two spin system, but we can easily extend the theory to many spin systems.

Figure 7 shows a simplified model of the measurement-feedback QNN. There are two cavities with an identical signal frequency ω_s and pump frequency $\omega_p = 2\omega_s$. The photon

annihilation operators of the signal and pump are denoted by $\hat{a}_{s1}, \hat{a}_{p1}, \hat{a}_{s2}, \hat{a}_{p2}$. There are also two external fields injected into the cavities. One is an excitation pump field ϵ_{pi} at ω_p . The other is a feedback signal field ϵ_{si} at ω_s , which is prepared by the measurement feedback circuit. The pump field and signal field have the loss rates denoted by γ_p and γ_s . To measure the in-phase component $\hat{X} = \hat{a} + \hat{a}^\dagger$ of the signal fields, a part of which is picked off and measured by homodyne detectors. The feedback signal is prepared based on the measurement results.

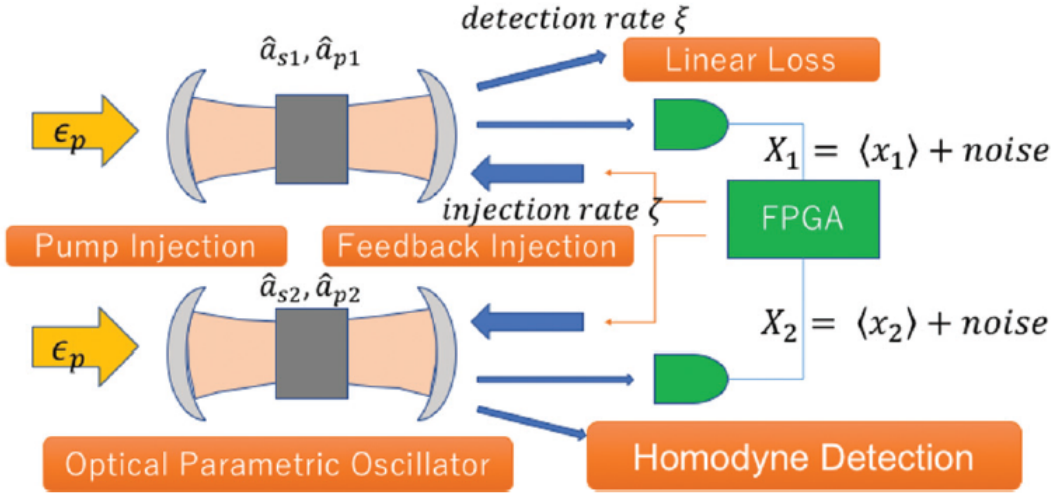


FIG. 7: A simple model for the CW measurement-feedback QNN [6].

5.2.1 Master Equations

Since the measurement-feedback process is local operation and classical communication (LOCC), the density matrix of the total system stays in a product state during a whole computation process:

$$\hat{\rho} = \hat{\rho}_1 \otimes \hat{\rho}_2 \quad (13)$$

where ρ_i is a density matrix of the DOPO i .

Our model is based on continuous time evolution, in which all the quantum operations proceed simultaneously, while the experimental measurement-feedback QNN [1, 2] is based on the discrete quantum operations. Modification of the present theory to discrete model is, however, straightforward.

We treat a DOPO and measurement feedback circuit, separately. The Hamiltonian of degenerate optical parametric oscillators (DOPO) is given by

$$\hat{H} = \hat{H}_{free} + \hat{H}_{int} + \hat{H}_{pump} + \hat{H}_{FB} + \hat{H}_{loss}, \quad (14)$$

$$\hat{H}_{free} = \hbar \sum_{i=1,2} \omega_s \hat{a}_{si}^\dagger \hat{a}_{si} + \omega_p \hat{a}_{pi}^\dagger \hat{a}_{pi}, \quad (15)$$

$$\hat{H}_{int} = \frac{i\hbar\kappa}{2} \sum_{i=1,2} \hat{a}_{si}^{\dagger 2} \hat{a}_{pi} - \hat{a}_{si}^2 \hat{a}_{pi}^\dagger, \quad (16)$$

$$\hat{H}_{pump} = i\hbar \sum_{i=1,2} \epsilon_p \hat{a}_{pi}^\dagger e^{-i\omega_p t} - \epsilon_p^* \hat{a}_{pi} e^{i\omega_p t}, \quad (17)$$

$$\hat{H}_{FB} = i\hbar \sum_{i=1,2} \epsilon_s \hat{a}_{si}^\dagger e^{-i\omega_s t} - \epsilon_s^* \hat{a}_{si} e^{i\omega_s t}, \quad (18)$$

$$\hat{H}_{loss} = \hbar \sum_{i=1,2} \hat{a}_{si}^\dagger \hat{\Gamma}_{si} + \hat{a}_{si} \hat{\Gamma}_{si}^\dagger + a_{pi}^\dagger \hat{\Gamma}_{pi} + a_{pi} \hat{\Gamma}_{pi}^\dagger, \quad (19)$$

where κ is a parametric coupling constant between the signal field and the pump field in a nonlinear crystal, and Γ_{pi} , Γ_{si} are external reservoir field operators which account for the injected fluctuation forces from the external environments. By tracing out these external fields by the standard Born-Markov approximation [12], we can obtain the master equation of the two DOPOs,

$$\begin{aligned} \frac{d\hat{\rho}}{dt} = & \sum_{i=1,2} i\hbar\omega_s \left[\hat{a}_{si}^\dagger \hat{a}_{si}, \hat{\rho} \right] + i\hbar\omega_p \left[\hat{a}_{pi}^\dagger \hat{a}_{pi}, \hat{\rho} \right] \\ & + \frac{\gamma_s}{2} \left(2\hat{a}_{si} \hat{\rho} \hat{a}_{si}^\dagger - \hat{a}_{si}^\dagger \hat{a}_{si} \hat{\rho} - \hat{\rho} \hat{a}_{si}^\dagger \hat{a}_{si} \right) \\ & + \frac{\gamma_p}{2} \left(2\hat{a}_{pi} \hat{\rho} \hat{a}_{pi}^\dagger - \hat{a}_{pi}^\dagger \hat{a}_{pi} \hat{\rho} - \hat{\rho} \hat{a}_{pi}^\dagger \hat{a}_{pi} \right) \\ & + \left[\epsilon_{si} e^{-i\omega_s t} \hat{a}^\dagger - \epsilon_{si}^* e^{i\omega_s t} \hat{a}_{si}^\dagger, \hat{\rho} \right] \\ & + \left[\epsilon_{pi} e^{-i\omega_p t} \hat{a}^\dagger - \epsilon_{pi}^* e^{i\omega_p t} \hat{a}_{pi}^\dagger, \hat{\rho} \right] \\ & + \frac{i\hbar\kappa}{2} \left[\hat{a}_{si}^{\dagger 2} \hat{a}_{pi} - \hat{a}_{si}^2 \hat{a}_{pi}^\dagger, \hat{\rho} \right]. \end{aligned} \quad (20)$$

By taking a rotating reference frame properly, we can eliminate the two terms in the first line.

To describe the non-unitary reduction of a wave function by the homodyne measurement,

Wiseman and Milburn proposed the following master equation [13, 14].

$$\begin{aligned} \frac{d\hat{\rho}}{dt} = & \sum_{i=1,2} \frac{\xi}{2} (2\hat{a}_{si}\hat{\rho}\hat{a}_{si}^\dagger - \hat{a}_{si}^\dagger\hat{a}_{si}\hat{\rho} - \hat{\rho}\hat{a}_{si}^\dagger\hat{a}_{si}) \\ & + \sqrt{\xi} \frac{dW}{dt} \left(\hat{a}_{si}\hat{\rho} + \hat{\rho}\hat{a}_{si}^\dagger - \langle \hat{a}_{si} + \hat{a}_{si}^\dagger \rangle \hat{\rho} \right), \end{aligned} \quad (21)$$

where $\langle \hat{X}_i \rangle = \langle \hat{a}_{si}^\dagger + \hat{a}_{si} \rangle$ is the expectation value of the in-phase amplitude of the signal fields and dW is a Wiener increment which satisfies

$$dW_i(t) \sim \mathcal{N}(0, dt), \quad (22)$$

$$\langle dW_i(t)dW_j(t') \rangle = 2\pi\delta_{ij}\delta(t-t'). \quad (23)$$

In this model, the measured value X_i is given by

$$X_i dt \propto \langle \hat{a}_{si}^\dagger + \hat{a}_{si} \rangle dt + \frac{dW_i}{\sqrt{\xi}}. \quad (24)$$

A feedback signal ϵ_{si} is now prepared according to the formula:

$$\epsilon_{si} = \zeta \sum J_{ij} X_j \quad (25)$$

where ζ is the strength of feedback coupling between DOPOs (Fig. 7).

Finally, we obtain the overall master equation of the measurement-feedback QNN by combining Eqs.(20) and (21):

$$\begin{aligned} \frac{d\hat{\rho}}{dt} = & \frac{\gamma_s + \xi}{2} (2\hat{a}_{si}\hat{\rho}\hat{a}_{si}^\dagger - \hat{a}_{si}^\dagger\hat{a}_{si}\hat{\rho} - \hat{\rho}\hat{a}_{si}^\dagger\hat{a}_{si}) \\ & + \frac{\gamma_p}{2} (2\hat{a}_{pi}\hat{\rho}\hat{a}_{pi}^\dagger - \hat{a}_{pi}^\dagger\hat{a}_{pi}\hat{\rho} - \hat{\rho}\hat{a}_{pi}^\dagger\hat{a}_{pi}) \\ & + [\epsilon_{si}e^{-i\omega t}\hat{a}^\dagger - \epsilon_{si}^*e^{i\omega t}\hat{a}_{si}^\dagger, \hat{\rho}] \\ & + [\epsilon_{pi}e^{-i\omega t}\hat{a}^\dagger - \epsilon_{pi}^*e^{i\omega t}\hat{a}_{pi}^\dagger, \hat{\rho}] \\ & + \frac{i\hbar\kappa}{2} [\hat{a}_{si}^\dagger\hat{a}_{pi} - \hat{a}_{si}^2\hat{a}_{pi}^\dagger, \hat{\rho}] \\ & + \sqrt{\xi} \frac{dW}{dt} \left(\hat{a}_{si}^\dagger\hat{\rho} + \hat{\rho}\hat{a}_{si} - \langle \hat{a}_{si}^\dagger + \hat{a}_{si} \rangle \hat{\rho} \right). \end{aligned} \quad (26)$$

5.2.2 Stochastic differential equations

A. Positive $P(\alpha, \beta)$ Representation

Positive $P(\alpha, \beta)$ representation of the density operator is defined by [15],

$$\hat{\rho} = \int \int P(\alpha, \beta) \hat{\Lambda}(\alpha, \beta) d^2\alpha d^2\beta, \quad (27)$$

where $\alpha, \beta \in \mathbb{C}$ and

$$\hat{\Lambda}(\alpha, \beta) = \frac{|\alpha\rangle \langle \beta|}{\langle \alpha | \beta \rangle} \quad (28)$$

is the off-diagonal projector in terms of coherent states, which form an overcomplete set. Here $|\alpha\rangle$ and $|\beta\rangle$ are the tensor product coherent states: $|\alpha\rangle = |\alpha_{s1}\rangle \otimes |\alpha_{p1}\rangle \otimes |\alpha_{s2}\rangle \otimes |\alpha_{p2}\rangle$ and $|\beta\rangle = |\beta_{s1}\rangle \otimes |\beta_{p1}\rangle \otimes |\beta_{s2}\rangle \otimes |\beta_{p2}\rangle$.

An important property of positive $P(\alpha, \beta)$ representation is that we can always define $P(\alpha, \beta)$ as a positive and real for arbitrary quantum states, which satisfies the normalization condition,

$$\int d^2\alpha d^2\beta P(\alpha, \beta) = 1. \quad (29)$$

Therefore, we can regard $P(\alpha, \beta)$ as a probability distribution function for finding the projector $|\alpha\rangle \langle \beta|$ in the density matrix.

Because the density matrix of the measurement-feedback QNN is always expressed as the product state of each DOPO density matrix, we can express $P(\alpha, \beta)$ as

$$P(\alpha, \beta) = P(\alpha_{s1}, \beta_{s1}, \alpha_{p1}, \beta_{p1}) P(\alpha_{s2}, \beta_{s2}, \alpha_{p2}, \beta_{p2}). \quad (30)$$

Therefore, we can describe the total system with the partial differential equation (PDE) for each DOPO.

Using the properties of the coherent states, we obtain the PDE of $P(\alpha_{si}, \beta_{si}, \alpha_{pi}, \beta_{pi})$,

$$\begin{aligned}
\frac{\partial P(\alpha, \beta)}{\partial t} = & \left[\sqrt{\xi} \{ \alpha_{si} + \beta_{si} - \langle \alpha_{si} + \beta_{si} \rangle \} \frac{dW}{dt} \right. \\
& - \frac{\partial}{\partial \alpha_{si}} \{ -(\gamma_s + \xi) \alpha_{si} + \kappa \beta_{si} \alpha_{pi} + \epsilon_{si} \} \\
& - \frac{\partial}{\partial \beta_{si}} \{ -(\gamma_s + \xi) \beta_{si} + \kappa \alpha_{si} \beta_{pi} + \epsilon_{si} \} \\
& - \frac{\partial}{\partial \alpha_{pi}} \left\{ -\gamma_p \alpha_{pi} - \frac{\kappa}{2} \alpha_{si}^2 + \epsilon_{pi} \right\} \\
& - \frac{\partial}{\partial \beta_{pi}} \left\{ -\gamma_p \beta_{pi} - \frac{\kappa}{2} \beta_{si}^2 + \epsilon_{pi} \right\} \\
& \left. + \frac{\partial^2}{\partial \alpha_{si}^2} \kappa \alpha_{pi} + \frac{\partial^2}{\partial \beta_{si}^2} \kappa \beta_{pi} \right] P(\alpha, \beta),
\end{aligned} \tag{31}$$

where

$$\langle \alpha_{si} \rangle = \int d^2 \alpha d^2 \beta \alpha_{si} P(\alpha, \beta), \tag{32}$$

$$\langle \beta_{si} \rangle = \int d^2 \alpha d^2 \beta \beta_{si} P(\alpha, \beta). \tag{33}$$

B. Stochastic differential equations and replicator dynamics

Except for the first line in Eq.(31), the PDE has an identical form as the Fokker-Planck equation. It is well established that the Fokker-Planck equation can be transformed to the stochastic differential equation (SDE) [12, 15],

$$\begin{aligned}
\begin{bmatrix} d\alpha_{si} \\ d\beta_{si} \end{bmatrix} = & \begin{bmatrix} -(\gamma_s + \xi) \alpha_{si} + \kappa \beta_{si} \alpha_{pi} + \epsilon_{si} \\ -(\gamma_s + \xi) \beta_{si} + \kappa \alpha_{si} \beta_{pi} + \epsilon_{si} \end{bmatrix} dt \\
& + \begin{bmatrix} \kappa \alpha_{pi} & 0 \\ 0 & \kappa \beta_{pi} \end{bmatrix}^{1/2} \begin{bmatrix} dW_{\alpha_i} \\ dW_{\beta_i} \end{bmatrix},
\end{aligned} \tag{34}$$

$$\begin{bmatrix} d\alpha_{pi} \\ d\beta_{pi} \end{bmatrix} = \begin{bmatrix} -\gamma_p \alpha_{pi} + \frac{\kappa}{2} \alpha_{si}^2 + \epsilon_{pi} \\ -\gamma_p \beta_{pi} + \frac{\kappa}{2} \beta_{si}^2 + \epsilon_{pi} \end{bmatrix} dt. \tag{35}$$

When we assume $\gamma_p \gg \gamma_s$, the pump fields decay more rapidly than the signal fields so that they follow the slow dynamics of the signal fields, which is called a slaving principle. Under

this assumption, we can eliminate the pump fields by assuming $d\alpha_{pi} = d\beta_{pi} = 0$,

$$\begin{aligned} \begin{bmatrix} d\alpha_{si} \\ d\beta_{si} \end{bmatrix} &= \begin{bmatrix} -(\gamma_s + \xi)\alpha_{si} + \frac{\kappa}{\gamma_p}\beta_{si}(\epsilon_{pi} - \frac{\kappa}{2}\alpha_{si}^2) + \epsilon_{si} \\ -(\gamma_s + \xi)\beta_{si} + \frac{\kappa}{\gamma_p}\alpha_{si}(\epsilon_{pi} - \frac{\kappa}{2}\beta_{si}^2) + \epsilon_{si} \end{bmatrix} dt \\ &+ \begin{bmatrix} \sqrt{\frac{\kappa}{\gamma_p}(\epsilon_{pi} - \frac{\kappa}{2}\alpha_{si}^2)}dW_{\alpha_i} \\ \sqrt{\frac{\kappa}{\gamma_p}(\epsilon_{pi} - \frac{\kappa}{2}\beta_{si}^2)}dW_{\beta_i} \end{bmatrix}. \end{aligned} \quad (36)$$

By introducing $\eta_i = g\alpha_{si}$, $\mu_i = g\beta_{si}$, $d\tau = \gamma_s dt$, $d\omega_{\eta_i} = \sqrt{\gamma_s}dW_{\alpha_i}$, $d\omega_{\mu_i} = \sqrt{\gamma_s}dW_{\beta_i}$, $p_i = \kappa\epsilon_{pi}/\gamma_s\gamma_p$, $f_i = g\epsilon_{si}/\gamma_s$, $g = \kappa/\sqrt{2\gamma_p\gamma_s}$, and $\xi' = \xi/\gamma_s$, we obtain the normalized SDE:

$$\begin{bmatrix} d\eta_i \\ d\mu_i \end{bmatrix} = \begin{bmatrix} -(1 + \xi')\eta_i + \mu_i(p_i - \eta_i^2) + f_i \\ -(1 + \xi')\mu_i + \eta_i(p_i - \mu_i^2) + f_i \end{bmatrix} d\tau + \begin{bmatrix} g\sqrt{p_i - \eta_i^2}d\omega_{\eta_i} \\ g\sqrt{p_i - \mu_i^2}d\omega_{\mu_i} \end{bmatrix}. \quad (37)$$

On the other hand, the first line of Eq.(31), which describes the reduction of wavepackets due to the measurement, cannot be simulated by the standard method using SDE. In previous works [13, 14], by assuming a measurement result is incidentally equal to the expectation value, they ignored this term. In this paper, we need to know the measurement effect to the evolution of the DOPO states, so that we keep the random measurement effect on $\eta_i(t)$ and $\mu_i(t)$ by accepting pseudo-random numbers dW .

Because the first line of Eq.(31) is a replicator equation, we extend the branching Brownian motion model [16], which is called replicator dynamics in our case. In replicator dynamics, the change of $P(\alpha, \beta)$ obeys

$$\frac{\partial P(\alpha, \beta)}{\partial t} = \lambda(\alpha, \beta)P(\alpha, \beta). \quad (38)$$

Here a Brownian particle at (α, β) is

$$\begin{cases} \text{copied with probability} & \lambda(\alpha, \beta) \quad (\lambda(\alpha, \beta) > 0) \\ \text{vanished with probability} & \lambda(\alpha, \beta) \quad (\lambda(\alpha, \beta) < 0), \end{cases} \quad (39)$$

where $\lambda(\alpha, \beta) = X_i - \langle X_i \rangle$.

Because the expectation values $\langle \alpha_{si} + \beta_{si} \rangle$ are needed to compute $\lambda(\alpha, \beta)$, we run many Brownian particles obeying the identical SDEs with stochastic noise but the identical measurement result X_i at the same time.

C. Gaussian approximation

In this section, we derive a Gaussian approximation method for the measurement-feedback QNN.

We start from the partial differential equation of signal fields after the adiabatic elimination of the pump field:

$$\begin{aligned}
\frac{\partial P(\alpha, \beta)}{\partial t} = & \left[\sqrt{\xi} \{ \alpha_{si} + \beta_{si} - \langle \alpha_{si} + \beta_{si} \rangle \} \frac{dW}{dt} \right. \\
& - \frac{\partial}{\partial \alpha_{si}} \left\{ -\gamma_s \alpha_{si} + \frac{\kappa}{\gamma_p} \beta_{si} \left(\epsilon_{pi} - \frac{\kappa \alpha_{si}^2}{2} \right) + \epsilon_{si} \right\} \\
& - \frac{\partial}{\partial \beta_{si}} \left\{ -\gamma_s \beta_{si} + \frac{\kappa}{\gamma_p} \alpha_{si} \left(\epsilon_{pi} - \frac{\kappa \beta_{si}^2}{2} \right) + \epsilon_{si} \right\} \\
& + \frac{\partial^2}{\partial \alpha_{si}^2} \frac{\kappa}{\gamma_p} \beta_{si} \left(\epsilon_{pi} - \frac{\kappa \alpha_{si}^2}{2} \right) \\
& \left. + \frac{\partial^2}{\partial \beta_{si}^2} \frac{\kappa}{\gamma_p} \alpha_{si} \left(\epsilon_{pi} - \frac{\kappa \beta_{si}^2}{2} \right) \right] P(\alpha, \beta).
\end{aligned} \tag{40}$$

By partial integration of Eq.(40), the equations of motion for the expectation values $\langle \alpha_{si} \rangle$ and $\langle \beta_{si} \rangle$ are obtained:

$$\begin{aligned}
d \langle \alpha_{si} \rangle = & \sqrt{\xi} \left[\langle \alpha_{si}^2 \rangle + \langle \alpha_{si} \beta_{si} \rangle - \langle \alpha_{si} \rangle^2 - \langle \alpha_{si} \rangle \langle \beta_{si} \rangle \right] dW \\
& + \left[-\gamma_s \langle \alpha_{si} \rangle + \frac{\kappa \epsilon_{si}}{\gamma_p} \langle \beta_{si} \rangle \right. \\
& \left. - \frac{\kappa^2}{2\gamma_p} \langle \alpha_{si}^2 \beta_{si} \rangle + \epsilon_{si} \right] dt,
\end{aligned} \tag{41}$$

$$\begin{aligned}
d \langle \beta_{si} \rangle = & \sqrt{\xi} \left[\langle \alpha_{si} \beta_{si} \rangle + \langle \alpha_{si}^2 \rangle - \langle \alpha_{si} \rangle \langle \beta_{si} \rangle - \langle \beta_{si} \rangle^2 \right] dW \\
& + \left[-\gamma_s \langle \beta_{si} \rangle + \frac{\kappa \epsilon_{si}}{\gamma_p} \langle \alpha_{si} \rangle \right. \\
& \left. - \frac{\kappa^2}{2\gamma_p} \langle \beta_{si}^2 \alpha_{si} \rangle + \epsilon_{si} \right] dt.
\end{aligned} \tag{42}$$

Similarly, we can derive the equations of motion for the higher order statistics, such as $\langle \alpha_{si}^2 \rangle$, $\langle \beta_{si}^2 \rangle$, and $\langle \alpha_{si} \beta_{si} \rangle$. Even though ϵ_{si} contains the statistics of other DOPOs such as $\langle \alpha_{sj} \rangle$ ($i \neq j$), $\langle \alpha_{si} \alpha_{sj} \rangle$ is reduced to $\langle \alpha_{si} \rangle \langle \alpha_{sj} \rangle$ since the total density matrix is separable. By changing the basis from $\langle \alpha_{si} \rangle, \langle \beta_{si} \rangle$ to $\langle X_i \rangle = \langle \alpha_{si} \rangle + \langle \beta_{si} \rangle, \langle iP_i \rangle = \langle \alpha_{si} \rangle - \langle \beta_{si} \rangle$, the equations of motion of $\langle X_i \rangle$, and $\langle P_i \rangle$ are acquired.

Though the dynamical equations are acquired, we can not simulate Eqs.(41) and (42)

immediately because of higher order terms like $\langle \alpha_{si}^2 \beta_{si} \rangle$. To avoid this difficulty, we consider the approximate wave function given by a displaced squeezed vacuum state

$$|\psi_i\rangle = \hat{D}(\mu_i) \hat{S}(\sigma_i^2) |0\rangle \quad (43)$$

where $\hat{D}(\mu_i) = \exp(\mu_i \hat{a}^\dagger - \mu_i^* \hat{a})$ is a displacement operator and $\hat{S}(\sigma_i^2) = \exp(1/2(\sigma_i^{2*} \hat{a}^2 - \sigma_i^2 \hat{a}^{\dagger 2}))$ is a squeezing operator. For simplicity, both μ_i and σ_i^2 are real. This approximation means that the DOPO state is always described by a pure squeezed state and higher order statistics have no effect to the dynamics of the system. By this approximation, we can finally get the dynamical equations of motion for the DOPOs:

$$\begin{aligned} d\mu_i = & \sqrt{\xi} \left(\sigma_i^2 - \frac{1}{4} \right) dW + \left[-\gamma_s \mu + \frac{\kappa}{\gamma_p} \epsilon_p \mu \right. \\ & \left. - \frac{\kappa^2}{2\gamma_p} \left(\mu^3 + \frac{\mu_i}{\sigma_i^2} \left(\sigma_i^2 - \frac{1}{4} \right) \left(3\sigma_i^2 - \frac{1}{4} \right) \right) + \epsilon_{si} \right] dt \end{aligned} \quad (44)$$

$$\begin{aligned} d\sigma_i^2 = & \left[-2\gamma_s \left(\sigma_i^2 - \frac{1}{4} \right) + \frac{2\kappa}{\gamma_p} \epsilon_p \left(\sigma_i^2 + \frac{1}{4} \right) \right. \\ & \left. - \frac{\kappa^2}{2\gamma_p} \left(\frac{5}{8} + 6\sigma_i^4 + 6\sigma_i^2 \mu_i^2 - \frac{1}{2} \sigma_i^2 + \frac{3}{2} \mu_i^2 - \frac{3}{32\sigma_i^2} \right) \right. \\ & \left. - 4\xi \left(\sigma_i - \frac{1}{4} \right)^2 \right] dt \end{aligned} \quad (45)$$

where,

$$\epsilon_{si} = \zeta \sum_j J_{ij} \left(\mu_j + \frac{dW}{\sqrt{\xi}} \right). \quad (46)$$

The first term in Eq.(44) describes the shift of the center position of the wave function by the measurement, while the last term in Eq.(45) describes the reduction of the variance by the measurement.

5.2.3 Numerical Simulation Results

In this section, we will show some numerical simulation results based on the exact theory with the CSDE (Eq.(37)) and the replicator dynamics (Eq.(38)), and compare them with the simulation results by the Gaussian approximation based on Eqs. (44) and (45).

A. 2 DOPO model

First, we study the system of two DOPOs with anti-ferromagnetic coupling. Figure 8(a) shows a time evolution of the average in-phase amplitude $\langle \hat{X}_i \rangle$, where $\gamma_s = 1$, $\gamma_p = 10$, $\kappa = 0.1$, $\xi = 0.1$, $\zeta = 0.3$ and $g = 0.02$. The external pump rate ϵ_p is linearly increased from 0 to 1.5 times the threshold pump rate ϵ_{th} . The two DOPOs are coupled by the anti-ferromagnetic interaction ($J_{ij} = -1$). Figure 8(b) expands $\langle \hat{X}_i \rangle$ vs. ϵ_p/ϵ_{th} near the decision making point. The two DOPOs point toward one ground state $|\uparrow\downarrow\rangle$ at one time but switch back to the other ground state $|\downarrow\uparrow\rangle$ at another time. This Brownian search process continues until the final decision is made at $\epsilon_p/\epsilon_{th} \simeq 0.9$. Note that the average photon number per DOPO is still on the order of one, i.e. the DOPO excitation level is microscopic, at this decision making instance, as shown in Fig. 8(c).

Figure 8(d) shows the measured values actually reported by homodyne detectors. We conclude that a correlation is formed between $\langle \hat{X}_1 \rangle$ and $\langle \hat{X}_2 \rangle$ at very early stages by the measurement feedback process, but the measured values are too noisy to disclose such a quantum search process. A final solution which the QNN will eventually report should be determined at the effective threshold pump rate $\epsilon_p/\epsilon_{th} = 1 - \zeta = 0.7$. We will discuss in the next section that the late decision making at $\epsilon_p/\epsilon_{th} = 0.9$ rather than 0.7 stems from the quantum tunneling.

The variance in the anti-squeezed in-phase amplitudes $\langle \Delta \hat{X}_1^2 \rangle$ is shown in Fig. 8(e), and the skewness $\langle \Delta \hat{X}_1^3 \rangle$ is shown in Fig. 8(f). Note that the DOPO wavefunction near and above threshold is clearly deviated from the Gaussian wavepacket, for which $\langle \Delta \hat{X}_1^3 \rangle = 0$ holds, but has a long tail toward the central potential barrier. The impact of this fact will be discussed in the next subsection.

Figure 9(a) and (b) show $\langle \hat{X}_i \rangle$ vs. ϵ_p/ϵ_{th} based on the Gaussian approximation method described above, while Fig. 9(c) shows the variances $\langle \sigma_i^2 \rangle$ vs. ϵ_p/ϵ_{th} . We can find the permanent negative correlation between $\langle \hat{X}_1 \rangle$ and $\langle \hat{X}_2 \rangle$ is formed already at the effective threshold pump rate $\epsilon_p/\epsilon_{th} = 0.7$. Compared with the results by the exact replicator dynamics, the variance $\langle \Delta \hat{X}_1^2 \rangle$ starts shrinking at $\epsilon_p/\epsilon_{th} = 0.7$ rather than $\epsilon_p/\epsilon_{th} = 0.9$ and the peak variance is smaller. We will discuss the meaning of this fact and the impact on the success rate in the next section.

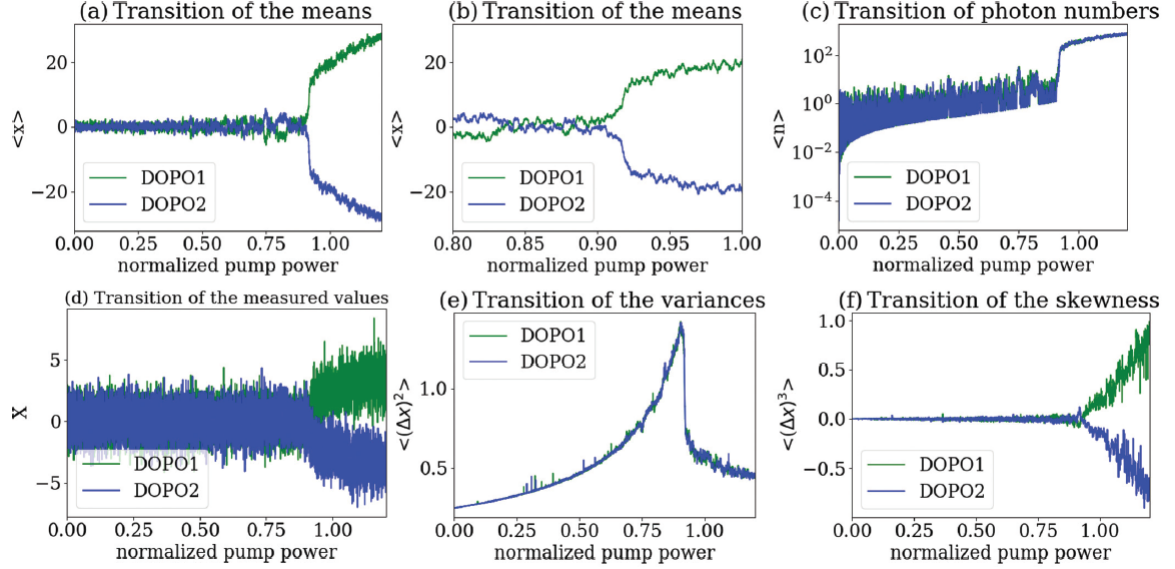


FIG. 8: (a) Time evolution of the expectation values of the in-phase components $\langle \hat{X}_1 \rangle$ and $\langle \hat{X}_2 \rangle$. This single trajectory of $\langle \hat{X}_1 \rangle$ and $\langle \hat{X}_2 \rangle$ are generated by the ensemble average over 10,000 Brownian particles. (b) Magnified picture of Fig. 8(a) near the decision making point. (c) Average photon numbers in the DOPO cavities. (d) Measured values of X_1 and X_2 by the homodyne detectors. (e) Variances σ_1^2 and σ_2^2 of the in-phase components. (f) Time evolution of the skewness of the in-phase components [6].

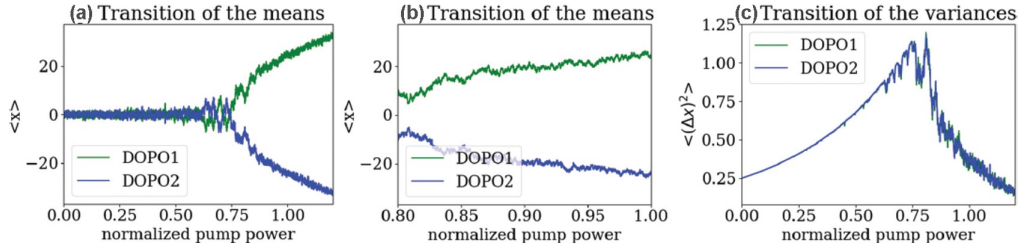


FIG. 9: (a) Time evolution of the expectation values of the in-phase components $\langle \hat{X}_1 \rangle$ and $\langle \hat{X}_2 \rangle$ under the Gaussian approximation. (b) Magnified view of Fig. 9(a) immediately after the effective threshold $\epsilon_p/\epsilon_{th} = 0.7$. (c) Variances of the in-phase components σ_1^2 and σ_2^2 under the Gaussian approximation [6].

B. 16 DOPO model

To reveal the unique capability of the QNN as an optimizer, we simulated a system of $N = 16$ DOPOs coupled by the nearest-neighbor anti-ferromagnetic interaction in one-dimensional ring geometry:

$$J_{ij} = \begin{cases} -1 & |i - j| = 1 \\ 0 & \text{otherwise.} \end{cases} \quad (47)$$

The two degenerate ground states for this model are $|\downarrow\uparrow \cdots \uparrow\rangle$ and $|\uparrow\downarrow \cdots \downarrow\rangle$. We compared the exact replicator dynamics with the Gaussian approximation. We also compare with an

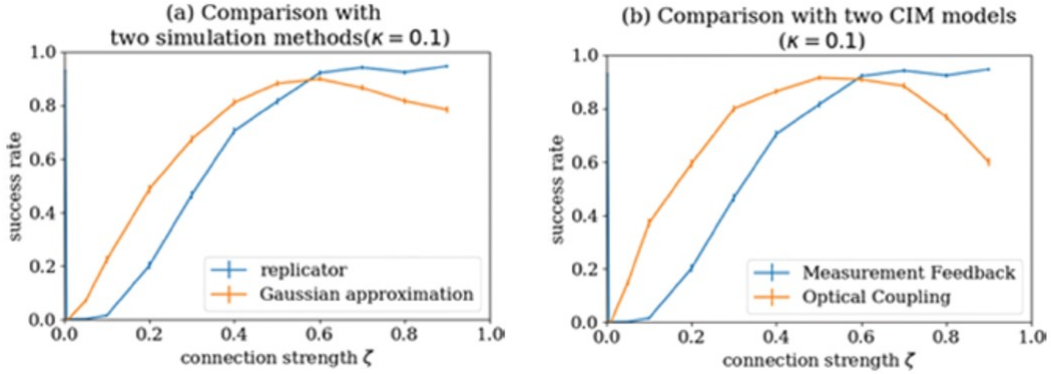


FIG. 10: (a) Success rate vs. connection strength ζ for the exact replicator dynamics model and Gaussian approximation. (b) Success rate vs. connection strength ζ for the measurement-feedback-based QNN and optical delay line coupling QNN [6].

optical delay line coupling QNN [8, 9].

Figure 10(a) shows the success rates in 1000 trials, where $\gamma_s = 1$, $\gamma_p = 10$, $\kappa = 0.1$, $\xi = 0.1$ and the injection rate ζ is changed from 0.001 to 1. ϵ_p is linearly increased from 0 to $1.2 \epsilon_{th}$. When the mutual coupling parameter ζ is small, the potential landscape for each DOPO field is almost symmetric with respect to $X = 0$ as shown in Fig. 11(a). In such a case, the measurement-induced wavepacket reduction and the feedback-induced wavepacket displacement play major roles in the solution search process. In this case, the tightly confined Gaussian wavepacket is more advantageous than the broadly spread exact wavepacket, because the latter introduces more noisy measurement results and so takes a longer time to reach a final result. However, when the mutual coupling parameter ζ is large, the potential for each DOPO field is highly asymmetric due to the strong injection field as shown in Fig. 11(b). In such a case, the non-Gaussian wavepacket induced quantum tunneling [17] plays an important role in the solution search process. In this case, the broadly spread (non-Gaussian) wavepacket is more advantageous than the tightly confined Gaussian wavepacket. The numerical simulation results in Fig. 10(a) confirm this trade-off relation.

Numerical results in Fig. 10(b) show that the optical delay line coupling QNN is more efficient than the measurement feedback QNN when ζ is small. However, in the case of $\zeta > 0.6$, the measurement feedback QNN has higher success rate than the optical delay line coupling QNN. When the connection strength ζ is close one, it means that the extracted signal field is boosted by a high-gain phase sensitive amplifier before it is injected back to the DOPO cavity (Fig. 1 of ref.[9]). This is necessary since the injection coupler has a very

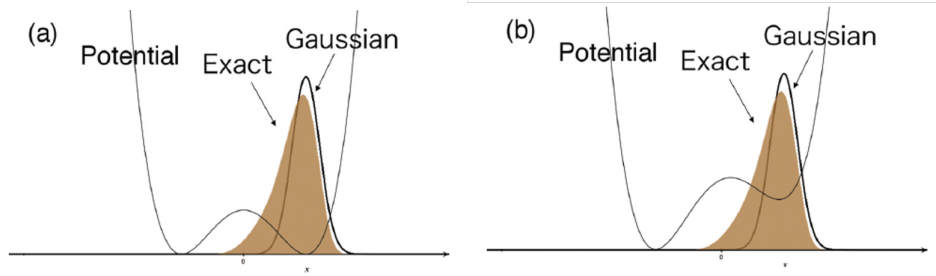


FIG. 11: (a) The almost symmetric potential for a DOPO field and the two wavepackets with a small ζ value. (b) The highly asymmetric potential for a DOPO field and the two wavepackets with a large ζ value [6].

small coupling constant. During this external amplification process, the vacuum fluctuation added to the extracted signal field is also amplified and contributes to the degradation of the degree of negative correlation among neighboring DOPOs. Because of this reason, there is an optimum coupling strength to maximize the degree of correlation in the optical delay line coupling QNN (see Fig. 3(b) of ref.[8]). The maximum success rate at $\zeta \simeq 0.5$ corresponds to this optimum coupling strength. In the case of the measurement-feedback-based QNN, the search mechanism is not the formation of correlation between DOPOs but the feedback signal-induced quantum tunneling so that a higher coupling strength ζ always improves the success rate.

5.3 Summary

Some of the important conclusions in Chapter V are summarized below.

1. The measurement feedback QNN is described by the two theoretical models. One is based on the density operator master equations and the other is based on the c -number stochastic differential equations.
2. The density operator master equation in in-phase amplitude eigen-state representation

for degenerate optical parametric amplification is given by

$$\begin{aligned}
\frac{d}{dt} \langle x | \hat{\rho} | x' \rangle &= g\beta (-z\partial_z - w\partial_w - 1) \langle x | \hat{\rho} | x' \rangle \\
&+ \frac{g^2}{8} (-z^2w^2 + 3(z^2 + w^2) \\
&+ (z^2 - w^2 + 8)(z\partial_z + w\partial_w) + 4(z^2 - 1)\partial_z^2 \\
&+ 4(w^2 - 1)\partial_w^2 + 4(z\partial_z - w\partial_w)(\partial_z^2 - \partial_w^2) \\
&- 4\partial_z^2\partial_w^2 \langle x | \hat{\rho} | x' \rangle.
\end{aligned} \tag{8}$$

The wavepacket reduction induced by optical homodyne detection is described by the projector,

$$\begin{aligned}
\hat{M} &= \langle x_m | \hat{U} | 0 \rangle \\
&= \int dx_i dx_f \pi^{-1/4} \delta(x_i - (\cos \theta x_f + \sin \theta x_m)) \\
&\times \exp\left(-\frac{1}{2}(-\sin \theta x_f + \cos \theta x_m)^2\right) |x_f\rangle \langle x_i|.
\end{aligned} \tag{11}$$

The feedback pulse injection is described by the displacement operator,

$$\hat{D}(\alpha\theta_f) = \exp(\alpha\theta_f\hat{a}^\dagger - \alpha^*\theta_f\hat{a}).$$

3. The c-number stochastic differential equations for describing the amplification, saturation and dissipation in a DOPO is given by

$$\begin{bmatrix} d\eta_i \\ d\mu_i \end{bmatrix} = \begin{bmatrix} -(1 + \xi')\eta_i + \mu_i(p_i - \eta_i^2) + f_i \\ -(1 + \xi')\mu_i + \eta_i(p_i - \mu_i^2) + f_i \end{bmatrix} d\tau + \begin{bmatrix} g\sqrt{p_i - \eta_i^2}d\omega_{\eta_i} \\ g\sqrt{p_i - \mu_i^2}d\omega_{\mu_i} \end{bmatrix}. \tag{37}$$

The replicator dynamics for describing the wavepacket reduction is given by

$$\frac{\partial P(\alpha, \beta)}{\partial t} = \lambda(\alpha, \beta)P(\alpha, \beta), \tag{38}$$

where a Brownian particle at (α, β) is

$$\begin{cases} \text{copied with probability} & \lambda(\alpha, \beta) \quad (\lambda(\alpha, \beta) > 0) \\ \text{vanished with probability} & \lambda(\alpha, \beta) \quad (\lambda(\alpha, \beta) < 0), \end{cases} \quad (39)$$

-
- [1] T. Inagaki et al., Science 354, 603 (2016).
- [2] P. McMahon et al, Science 354, 614 (2016).
- [3] Y. Yamamoto and Y. Watanabe, Phys. Rev. A 38, 3556 (1988).
- [4] W. H. Richardson et al., Phys. Rev. Lett. 66, 1963 (1991).
- [5] A. Yamamura et al., Phys. Rev. A 96, 053834 (2017) .
- [6] T. Shoji et al., Phys. Rev. A 96, 053833 (2017) .
- [7] When we define the in-phase and quadrature-phase amplitude as $x = (a + a^\dagger) / \sqrt{2}$ and $p = (a - a^\dagger) / \sqrt{2}i$, they satisfy the commutation relation $[x, p] = i$ and the uncertainty principle is given by $\langle \Delta x^2 \rangle \langle \Delta p^2 \rangle \geq 1/4$.
- [8] K. Takata et al., Phys. Rev. A 92, 043821 (2015) .
- [9] D. Maruo et al., Phys. Scr. 91, 083010 (2016).
- [10] H. P. Breuer and F. Petruccione, The Theory of Open Quantum Systems (Oxford University Press, Oxford, 2007).
- [11] R. Hamerly et al., Int. J. Mod. Phys. B 30, 1630014 (2016).
- [12] C. Gardiner, Stochastic Methods: A Handbook for the Natural and Social Sciences (Springer-Verlag, Berlin, Heidelberg, 2009).
- [13] H. M. Wiseman and G. J. Milburn, Phys. Rev. Lett. 70, 548 (1993).
- [14] H. M. Wiseman and G. J. Milburn, Phys. Rev. A 47, 642 (1993).
- [15] P. D. Drummond and C. W. Gardiner, J. Phys. A 13, 2353 (1980).
- [16] S. P. Lalley and T Sellke, The Annals of Probability 15, 1052 (1987).
- [17] P. Kinsler and P. D. Drummond, Phys. Rev. A 43, 6194 (1991).

Written by Y. Yamamoto, A. Yamamura and T. Shoji

version 1